Reconfigurable Magnetic Resonance-Coupled Wireless Power Transfer System

Zhigang Dang, *Student Member, IEEE*, Yuan Cao, *Student Member, IEEE*, and Jaber A. Abu Qahouq, *Senior Member, IEEE*

***Abstract*—This paper presents a method for a reconfigurable magnetic resonance-coupled wireless power transfer (R-MRC-WPT) system in order to achieve higher transmission efficiency under various transmission distance and/or misalignment conditions. Higher efficiency, longer transmission distance, and larger misalignment tolerance can be achieved with the presented R-MRC-WPT system when compared to the conventional four-coil MRC-WPT (C-MRC-WPT) system. The reconfigurability in the R-MRC-WPT system is achieved by adaptively switching between different sizes of drive loops and load loops. All drive loops are in the same plane and all load loops are also in the same plane; this method does not require mechanical movements of the drive loop and load loop and does not result in the system volume increase. Theoretical basis of the method for the R-MRC-WPT system is derived based on a circuit model and an analytical model. Results from a proof-of-concept experimental prototype, with transmitter and receiver coil diameter of 60 cm each, show that the transmission efficiency of the R-MRC-WPT system is higher than the transmission efficiency of the C-MRC-WPT system and the capacitor tuning system for all distances up to 200 cm (∼3.3 times the coil diameter) and for all lateral misalignment values within 60 cm (one coil diameter).**

***Index Terms*—Frequency splitting, inductive power transfer, magnetic resonance coupling (MRC), misalignment tolerance, reconfigurable system, transmission efficiency, wireless charging, wireless power transfer (WPT).**

I. Introduction

WIRELESS power transfer (WPT), as a reemerging technology, has several promising and potential applications such as consumer electronics, medical implants, and electric vehicle (EV) charging [1]–[3]. Electromagnetic-based WPT includes radiative (far-field) and nonradiative (near-field) methods. Some radiative WPT systems utilize microwave or laser beam to transfer power for directive long distance but with very limited efficiency [4], [5]. Nonradiative inductive WPT (IPT) can be used to transfer significant amount of power within a short distance, which is usually less than one coil diameter [3], [6]–[14]. The IPT system usually employs a two-coil system, which includes a transmitter coil (Tx) and a receiver coil (Rx). This usually aims to maximize total system energy efficiency (which is referred to as maximum energy efficiency principle in [15]). The short-range IPT system usually employs ferrite structures in Tx and Rx to achieve stronger magnetic coupling. It is able to transmit large amount of power with high total system energy efficiency up to ∼85% to 90%, which makes it suitable for the applications such as EV charging [3], [7]–[14].

Magnetic resonance coupling, as a special form of inductive coupling, utilizes magnetically coupled resonators (Tx coil and Rx coil) to transfer power wirelessly [16]–[30]. Magnetic resonance-coupled wireless power transfer (MRC-WPT) is suitable for mid-range low-power applications such as consumer electronics charging where the transmission distance might be longer than one Tx coil diameter. MRC-WPT also has advantages in tolerating larger angular and lateral misalignments [17], [18], [20], [21]. In the mid-range WPT applications, if system energy efficiency is not the major concern, the maximum power transfer principle can be adopted in order to maximize the power delivered to the load and extend the transmission distance at the expense of the system energy efficiency [15]–[19]. The authors in [15] discussed the difference between the maximum power transfer principle and the maximum system energy efficiency principle and how they are related to WPT systems. Two-coil WPT systems and four-coil WPT systems are commonly used in MRC-WPT systems. For both two-coil and four-coil WPT systems, higher quality factors for both Tx and Rx and stronger magnetic coupling between Tx and Rx are desired in order to maintain higher transmission efficiencies within longer transmission distances [16]–[21].

A two-coil MRC-WPT system improves transmission efficiency and/or transmission distance further by optimizing the series and parallel (shunt) capacitances in the Tx and Rx coils. Various WPT circuit topologies with different resonant types such as series–series, series–parallel, parallel–series, and parallel–parallel have been discussed in the literature [3], [31]. Some literature such as [31] concluded that the use of series-shunt mixed-resonant coupling for the two-coil WPT system allows better flexibility for optimizing the transmission efficiency at different distances.

A four-coil MRC-WPT system, which includes a drive loop, a Tx coil, a Rx coil, and a load loop, has been attracting great interests since being explored in [16], which shows a four-coil system with 60-cm diameter for Tx and Rx that can transmit 40 W over a distance of 2 m. For this later system, the Tx coil to Rx coil transmission efficiency is 40% and the total system energy efficiency is 15%. In four-coil systems, the Tx and Rx are usually open-ended self-resonating coils that are not directly connected to the source and load [15]–[21], and

Manuscript received October 1, 2014; revised January 18, 2015 and March 14, 2015; accepted March 30, 2015. Date of publication April 13, 2015; date of current version July 10, 2015. Recommended for publication by Associate Editor O. C. Onar.

The authors are with the Department of Electrical and Computer Engineering, College of Engineering, University of Alabama, Tuscaloosa, AL 35487, USA (e-mail: zdang@crimson.ua.edu; ycao19@crimson.ua.edu; jaberq@ieee.org).

Color versions of one or more of the figures in this paper are available online at http://ieeexplore.ieee.org.

Digital Object Identifier 10.1109/TPEL.2015.2422776

they are inductively coupled to a drive-loop and a load-loop that are connected to source and load, respectively. This is unlike the case for two-coil systems where Tx and Rx are directly connected to the source and load circuit. Therefore, when both Tx and Rx coils operate at resonance and both of them have the same resonance frequency, a higher quality factor can be obtained for Tx and Rx in a four-coil system compared to a two-coil system as explained in [19] and [20]. Meanwhile, the additional two loop-to-coil coupling factors (drive loop to Tx coupling factor and Rx to load loop coupling factor) in the four-coil system provide higher degree of freedom for design optimization to achieve impedance matching, when compared to the two-coil system, in order to extend the transmission distance [15], [32].

In a four-coil MRC-WPT system, as long as the coupling factor between Tx and Rx (k_{TR}) exceeds a threshold value (k_c), i.e., Rx is within the overcoupled region, frequency splitting can exist and nearly constant maximum transmission efficiency can be maintained [17]–[21]. In [17], a frequency tuning technique is demonstrated to compensate for the efficiency variation (resulted from frequency splitting) when the transmission distance and/or Tx to Rx orientation are varied. By doing so, maximum transmission efficiencies are adaptively tracked. Similar frequency tuning technique is used in [18] to maintain a high-efficiency region for a laterally misaligned MRC-WPT system with various vertical distances between Tx and Rx. Combination of the frequency tuning and other techniques can further optimize transmission efficiency and/or extend transmission distance. Frequency tuning is combined with a variable coupling technique in [33], which varies the loop-to-coil coupling factors (drive loop to Tx coil coupling factor and Rx coil to load loop coupling factor) by varying loop-coil distances (distance between the drive loop and Tx coil and distance between load loop and Rx coil). This technique improves transmission efficiencies within a distance of 100 cm compared with fixed coupling system. Similarly, [34] varies the loop-coil coupling factor by rotating the drive loop and load loop around the axis of the Tx and Rx. This results in improving transmission efficiencies and reducing cross coupling factors (drive loop to load loop coupling factor, drive loop to Rx coupling factor, and Tx to load loop coupling factor). However, both techniques (which are referred to as the mechanical tuning methods in the rest of this paper) require mechanical movement of the drive loop and load loop, which increases the system volume and complexity.

This paper presents a method for a reconfigurable R-MRC-WPT system in order to obtain maximum achievable transmission efficiency under various transmission distance (DIS) and/or misalignment (MIS) conditions. Higher efficiency, longer transmission distance, and larger misalignment tolerance can be achieved with the presented R-MRC-WPT system when compared to the conventional four-coil MRC-WPT (C-MRC-WPT) system. The reconfigurability in the R-MRC-WPT system is achieved by adaptively switching between different sizes of drive loops and load loops. All drive loops are in the same plane and all load loops are also in the same plane, this method does not require mechanical movements of the drive loop and load loop and does not result in system volume increase. The presented R-MRC-WPT system includes an array of drive loops, one Tx coil, one Rx coil, and an array of load loops. It adaptively switches between different system's configurations and tune the frequency of operation in order to obtain the maximum transmission efficiencies under various DIS and MIS conditions. The R-MRC-WPT is different from adding external tuning circuits such as capacitors and/or inductors to a C-MRC-WPT system with fixed size of drive/load loop. This is because external tuning circuits can only move the system operating point back to the impedance matching point to achieve the maximum possible efficiency at a given DIS (or set of conditions) for the fixed design structure, while switching between different loops reconfigures the system such that it switches between different designs or operating/efficiency curves that are more optimized for different DIS and MIS conditions.

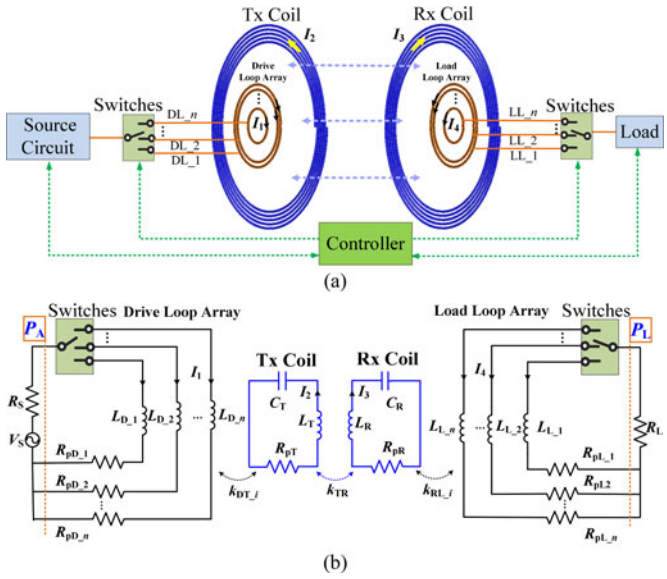

Fig. 1. (a) Physical model and (b) simplified circuit model of the R-MRC-WPT system ($i = 1, 2, \ldots, n$).

Section II presents the R-MRC-WPT system and derives its theoretical basis based on an in depth analysis of a circuit model and an analytical model. Proof-of-concept experimental prototype results are presented in Section III. Section IV discusses the uses of ferrite and litz wire in the R-MRC-WPT system and the conclusion is given in Section V.

II. Proposed Reconfigurable MRC-WPT System

A. R-MRC-WPT System

Fig. 1(a) illustrates the physical model of the R-MRC-WPT system. The system includes an array of drive loops with n separate single loops (from DL_1 to DL_n) placed in the same plane, a Tx coil, a Rx coil, and an array of load loops with n separate single loops (from LL_1 to LL_n) placed in the same plane. There is a switch array attached to the drive-loop array and another switch array attached to the load-loop array. A controller obtains information from load side and source side to decide which drive loop and load loop should be turned

ON (or connected) under a given operating condition such as a DIS and/or a MIS condition. The decision making is based on the calculation of transmission efficiency, which is defined as the load power (P_L) divided by the maximum available power at drive-loop (P_A), i.e., P_L/P_A. P_L and P_A are marked on Fig. 1(b). Note that transmission efficiency is different from the total system energy efficiency as clarified in [15]. When switching between different loops using the switch-array, a switch must be turned ON in order to keep at least one loop connected before another switch is turned OFF in order to avoid sudden interruption of current and power flow thorough the WPT system.

This paper focuses on the symmetrical system analysis, i.e., DL_*i* ($i = 1, 2 \ldots, n$) at Tx side and LL_*i* ($i = 1, 2 \ldots, n$) at Rx side are turned ON and OFF simultaneously such that the radii of the drive and load loops are equal for each configuration. The configuration of the R-MRC-WPT system when DL_*i* and LL_*i* are turned ON is referred to as Configuration-*i*. Tx and Rx are magnetically coupled to the DL_*i* and LL_*i*, respectively. DL_*i* and LL_*i* are connected to the power source and the load, respectively. Tx and Rx are symmetrical self-resonators (no external capacitors are connected to them) and they are linked through magnetically coupled resonances.

The adaptive reconfiguration for the MRC-WPT system is realized by switching between different loops such that higher efficiency can be obtained for various transmission ranges and misalignment conditions (which is explained in detail next). No mechanical movements are required in the R-MRC-WPT system. Since all drive loops are in the same plane and all load loops are in the same plane, the R-MRC-WPT system does not result in volume increased when compared to the C-MRC-WPT system. Therefore, the R-MRC-WPT system does not suffer from the disadvantages of mechanically tuned WPT systems where mechanical movement is required and volume is increased.

Fig. 1(b) shows the simplified lumped element circuit model for the system illustrated in Fig. 1(a), where the capacitors shown with Tx and Rx coils represent the lumped model of the parasitic capacitances in the self-resonating Tx and Rx spiral coils. DL_*i* is modeled as an inductor L_{D_i} with a series parasitic resistor R_{pD_i}. DL_*i* is connected to an ac voltage source *V*s (with a source resistance *R*s) from one side and is inductively coupled to Tx with a coupling factor of k_{DT_i} from the other side. The coupling factor is defined in (1), where M_{xy} is the mutual inductance, and L_x and L_y are self-inductances. Tx and Rx are modeled as two separate series *LCR* resonators. Rx is coupled with Tx by a coupling factor of k_{TR}, which is inversely proportional to DIS^3 [16], [17]. The self-resonance frequencies of two resonators are determined by (2) and the angular resonance frequency is defined as $\omega_o = 2\pi f_o$. Similar to DL_*i*, LL_*i* is modeled as an inductor L_{L_i} with a series parasitic resistor R_{pL_i}. LL_*i* is connected to load R_L from one side and is inductively coupled to Rx through a coupling factor of k_{RL_i} from the other side. No external capacitors are connected to drive and load loops, and parasitic capacitances of drive and load loops are negligible

$$k_{xy} = \frac{M_{xy}}{\sqrt{L_x L_y}} \tag{1}$$

$$f_o = \frac{1}{2\pi\sqrt{\mathrm{LC}}}. \tag{2}$$

B. Circuit Model Analysis

In this section, some important equations for the R-MRC-WPT system are derived based on the simplified circuit model as shown in Fig. 1(b). To simplify analysis, all cross couplings are ignored, only symmetrical system is analyzed, and only one DL_*i* and one LL_*i* are turned ON in each configuration (configuration-*i*). Based on this, all circuit model parameters can be simplified as in (3). The impedance of each loop could then be expressed as in (4), where Z_{D_i} and Z_{L_i} are the impedances of DL_*i* and LL_*i*, respectively. These two impedances are equal in the symmetrical case and are renamed as $Z_{\mathrm{loop}\_i} = Z_{D\_i} = Z_{L\_i}$. Z_T and Z_R are the impedances of Tx and Rx, respectively. These two impedances are also equal in the symmetrical case and are renamed as $Z_{\mathrm{coil}} = Z_T = Z_R$. The current in each loop could be determined as given by (5) by using Kirchhoff's Voltage Law. The voltage ratio V_L/V_S as a function of ω and k_{TR} can then be solved for as given by (6), where $\omega = 2\pi f$. In (3) to (6), $i = 1, 2 \ldots, n$

$$\begin{cases} R_{pD\_i} = R_{pL\_i} = R_{\mathrm{loop}\_i}, L_{D\_i} = L_{L\_i} = L_{\mathrm{loop}\_i} \\ L_T = L_R = L_{\mathrm{coil}}, C_T = C_R = C_{\mathrm{coil}} \\ R_{pT} = R_{pR} = R_{\mathrm{coil}}, R_S = R_L = R_o \\ k_{DT\_i} = k_{RL\_i} = k_{lc\_i}, M_{DT\_i} = M_{RL\_i} = M_{lc\_i} \end{cases} \tag{3}$$

$$\begin{cases} Z_{\mathrm{loop}\_i} = Z_{D\_i} = Z_{L\_i} = R_o + R_{\mathrm{loop}\_i} + j\omega L_{\mathrm{loop}\_i} \\ Z_{\mathrm{coil}} = Z_T = Z_R = R_{\mathrm{coil}} + j\omega L_{\mathrm{coil}} + \dfrac{1}{j\omega C_{\mathrm{coil}}} \end{cases} \tag{4}$$

$$\begin{bmatrix} Z_{D\_i} & j\omega M_{lc\_i} & 0 & 0 \\ j\omega M_{lc\_i} & Z_T & -j\omega M_{TR} & 0 \\ 0 & -j\omega M_{TR} & Z_R & j\omega M_{lc\_i} \\ 0 & 0 & j\omega M_{lc\_i} & Z_{L\_i} \end{bmatrix} \begin{bmatrix} I_1 \\ I_2 \\ I_3 \\ I_4 \end{bmatrix} = \begin{bmatrix} V_S \\ 0 \\ 0 \\ 0 \end{bmatrix} \tag{5}$$

$$\frac{V_L}{V_S} = \frac{j\omega^3 k_{TR} k_{lc\_i}^2 L_{\mathrm{coil}}^2 L_{\mathrm{loop}\_i} R_L}{(\omega^2 k_{lc\_i}^2 L_{\mathrm{coil}} L_{\mathrm{loop}\_i} + Z_{\mathrm{coil}} Z_{\mathrm{loop}\_i})^2 + \omega^2 k_{TR}^2 \left(L_{\mathrm{coil}} Z_{\mathrm{loop}\_i}\right)^2} \tag{6}$$

The voltage ratio in (6) can directly be used to calculate the equivalent S_{21} scattering parameter (7), which then can be used in (8) to evaluate the transmission efficiency (η) for the MRC-WPT system when source and load impedances are equal [15], [17], [19]. Mathematical proofs for (7) and (8) are provided in Appendix I. The series quality factor of the Tx and Rx coils is defined by (9). The quality factor of drive/load loop at the self-resonance frequency of Tx/Rx is defined in (10). In (10) to (12-3), $i = 1, 2 \ldots, n$

$$S_{21} = 2\frac{V_L}{V_S} \tag{7}$$

$$\eta = |S_{21}|^2 \times 100\% \tag{8}$$

$$Q_{\text{coil}} = \frac{1}{R_{\text{coil}}}\sqrt{\frac{L_{\text{coil}}}{C_{\text{coil}}}} = \frac{1}{\omega_o R_{\text{coil}} C_{\text{coil}}} = \frac{\omega_o L_{\text{coil}}}{R_{\text{coil}}} \tag{9}$$

$$Q_{\text{loop\_}i}\,|_{\omega=\omega_o} = \frac{\omega_o L_{\text{loop\_}i}}{R_o + R_{\text{loop\_}i}}. \tag{10}$$

Using the same derivation techniques as in [17] and [19], for configuration-*i*, the critical coupling factor (k_{c_i}), critical $|S_{21}|(|S_{21}|_{c\_i})$, and transmission efficiency ($\eta_{\_i}$) can be derived as given by (11), (12-1), and (12-2), respectively. Note that k_{c_i} is the smallest Tx to Rx coupling factor (k_{TR}) within which the system is able to maintain nearly constant $\eta_{\_i}$ when configuration-*i* is selected. In other words, as long as $k_{TR} \geq k_{c\_i}$, nearly constant $\eta_{\_i}$ can be maintained in the corresponding transmission distance DIS_*i*. When $k_{TR} > k_{c\_i}$, the system operates in the overcoupled region and there exists frequency splitting. When $k_{TR} = k_{c\_i}$, the system operates at the critical coupling point, at which the two resonance frequencies merge into one. When $k_{TR} < k_{c\_i}$, the system operates in the undercoupled region where there is no frequency splitting anymore. In the undercoupled region, the $\eta_{\_i}$ quickly decreases as Rx moves away from Tx. Therefore, a smaller k_{c_i} (which corresponds to a longer DIS_*i*) and a larger $|S_{21}|_{c\_i}$ (which corresponds to a higher $\eta_{\_i}$) are desired in order to extend transmission distance with higher transmission efficiencies

$$k_{c\_i} = \frac{1}{Q_{\text{coil}}} + k_{lc\_i}^2 \frac{Q_{\text{loop\_}i} R_o}{Z_{\text{loop\_}i}} = \frac{1}{Q_{\text{coil}}} + k_{lc\_i}^2 \frac{\omega}{\frac{R_o}{L_{\text{loop\_}i}} + j\omega} \tag{11}$$

$$|S_{21}|_{c\_i} = \frac{k_{lc\_i}^2 Q_{\text{loop\_}i} R_o}{k_{c\_i} Z_{\text{loop\_}i}} \tag{12-1}$$

$$\eta_{\_i} = |S_{21}|_{c\_i}^2 = \left(\frac{k_{lc\_i}^2 Q_{\text{loop\_}i} R_o}{k_{c\_i} Z_{\text{loop\_}i}}\right)^2 \tag{12-2}$$

$$\eta_{\_i} = |S_{21}|_{c\_i}^2 = \left(\frac{Q_{\text{coil}} R_o^2}{Q_{\text{coil}} R_o Z_{\text{loop\_}i} + \frac{Z_{\text{loop\_}i}^2}{Q_{\text{loop\_}i} k_{lc\_i}^2}}\right)^2 \tag{12-3}$$

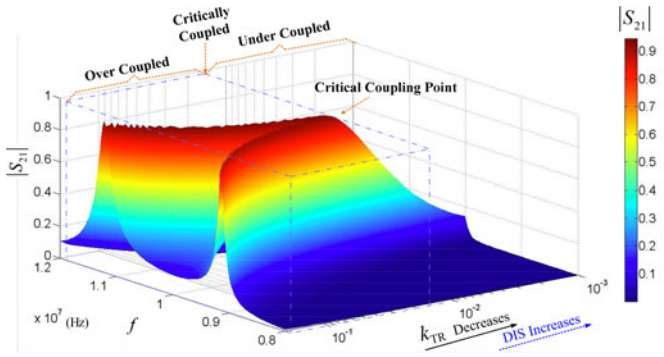

Fig. 2. Three-dimensional view of $|S_{21}|$ as functions of frequency and k_{TR}.

TABLE I
DESIGN EXAMPLE PARAMETER VALUES [17]

Parameters	Values	Parameters	Values
f_o	10 MHz	$R_{pD} = R_{pL} = R_{\text{loop}}$	0.25 Ω
$R_S = R_L = R_o$	50 Ω	Q_{loop}	1.25
$L_T = L_R = L_{\text{coil}}$	20.0 μH	$k_{DT} = k_{RL} = k_{lc}$	0.1
$C_T = C_R = C_{\text{coil}}$	12.6 pF	k_{TR}	$0 < k_{TR} < 1$
$R_{pT} = R_{pR} = R_{\text{coil}}$	1 Ω	Frequency sweep	8 to 12 MHz
$L_D = L_L = L_{\text{loop}}$	1.0 μH	-	-

A 3-D view of $|S_{21}|$ as functions of frequency and k_{TR} is plotted in Fig. 2 by using the example parameters shown in Table I, where the *x*-axis is the frequency, the *y*-axis is k_{TR} value, and the *z*-axis is the value of $|S_{21}|$. As expected, frequency splitting is observed in the overcoupled region when $k_{TR} > k_{c\_i}$, within which nearly constant $|S_{21}|$ value is maintained. With the decrease of k_{TR}, the two frequency peaks gradually merge into one at the critical coupling point when $k_{TR} = k_{c\_i}$. When k_{TR} decreases further with the increase of DIS, $|S_{21}|$ value decreases quickly.

It can be observed from (11) and (12-2) that a larger Q_{coil} contributes to both a smaller k_{c_i} and a larger $|S_{21}|_{c\_i}$. Based on this, maximizing the value of Q_{coil} can result in increasing the values of DIS_i and $\eta_{\_i}$. Other factors that affect k_{c_i} and $\eta_{\_i}$ include k_{lc_i}, $Q_{\text{loop\_}i}$, $Z_{\text{loop\_}i}$, and R_o. R_o is fixed at 50 Ω in this analysis. Moreover, it can be observed from (4) and (10) that $Z_{\text{loop\_}i}$ and $Q_{\text{loop\_}i}$ are all directly proportional to the $L_{\text{loop\_}i}$. In order to clarify the relationship between the physical dimensions of drive/load loop and $L_{\text{loop\_}i}$, k_{lc_i}, k_{c_i}, $\eta_{\_i}$, and DIS_i, the analytical model of the R-MRC-WPT system is derived and discussed next in this paper.

C. Analytical Model Analysis

The value of the self-inductance of a single conductor loop is given by (13) [35], where *r* is the radius of the loop, μ_o is the vacuum permeability, μ_r is the relatively permeability (in the case of air $\mu_r \approx 1$), and *d* is the diameter of the conductor. It can be observed from (13) that the inductance $L_{\text{loop\_}i}$ of the *i*th

drive/load loop is directly proportional to its radius r_i

$$L_{\text{loop}} = \mu_0 \mu_r r \left[\text{In} \left(\frac{16r}{d} \right) - 2 \right]. \tag{13}$$

However, the relationship between k_{lc_i} and r_i is not easily observable because when varying r_i, both self-inductance L_{loop_i} and mutual inductance M_{lc_i} change. In order to study how k_{lc_i} varies as a function of r_i, an analytical model of k_{lc_i} as a function of r_i is derived. The mutual inductance of two planar loops is given by (14) based on Neumann's equation [36], where r_1 and r_2 are radii of two different loops, respectively, and *h* is the distance between the two loops

$$M = \frac{\mu_0 \pi r_1^2 r_2^2}{2(r_1^2 + r_2^2 + h^2)^{3/2}} \left(1 + \frac{15}{32}\gamma^2 + \frac{315}{1024}\gamma^4 \right) \tag{14-1}$$

$$\gamma = 2r_1 r_2 / (r_1^2 + r_2^2 + h^2). \tag{14-2}$$

The multiturn spiral coil can be modeled as concentric loops and its self-inductance can then be calculated from (15), which can be used to calculate the inductance of the Tx/Rx coil. In (15), *n* is the number of turns and L_j is the inductance of *j*th turn in the Tx/Rx coil, which can be calculated from (13)

$$L_{\text{coil}} = \sum_{j=1}^{n} L_j + 2 \times \sum_{a=1}^{n-1} \sum_{b=a+1}^{n} M_{ab}. \tag{15}$$

The mutual inductance between two coils can be derived as in (16) [36], where n_1 and n_2 are the number of turns for the two coils, M_{ab} represents the mutual inductance between the *a*th turn of one coil and the *b*th turn of the other coil. M_{ab} can be calculated from (14)

$$M = \sum_{a=1}^{a=n_1} \sum_{b=1}^{b=n_2} M_{ab}. \tag{16}$$

Based on (1) and (13)–(16), k_{lc_i} can be expressed as in (17), where M_{lc_i} is the mutual inductance between *i*th drive/load loop and Tx/Rx coil, L_{loop_i} is the inductance of *i*th drive/load loop, n_1 is the number of turns of the drive/load loop (which is equal to 1), and n_2 is the number of turns of Tx/Rx coil

$$k_{lc\_i} = \frac{M_{lc\_i}}{\sqrt{L_{\text{loop}\_i} \times L_{\text{coil}}}} = \frac{\sum_{a=1}^{a=n_1} \sum_{b=1}^{b=n_2} M_{ab}}{\sqrt{L_{\text{loop}\_i} \times \left(\sum_{b=1}^{n_2} L_b + 2 \times \sum_{a=1}^{n_2-1} \sum_{b=a+1}^{n_2} M_{ab} \right)}} \tag{17}$$

From (17), k_{lc_i} as a function of r_i can be derived as in (18), as shown at the bottom of the page, where r_b is the radius of the *b*th turn of Tx/Rx coil and d_{lc} is the distance between drive/load loop and Tx/Rx coil.

In order to be able to clearly observe the relationship between k_{lc_i} and r_i, k_{lc_i} as a function of r_i is plotted as shown in Fig. 3 by using the analytical model in (18), where $0 < r_i$ outer radius of Tx/Rx coil (= 30 cm) and the other parameters are given in Table II. It can be observed from Fig. 3 that k_{lc_i} is directly

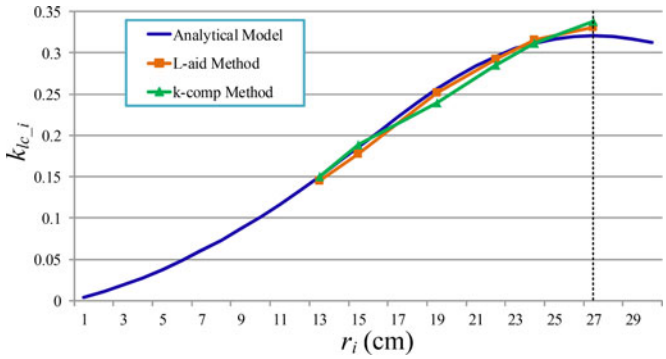

Fig. 3. k_{lc_i} as a function of r_i.

TABLE II
PARAMETER SPECIFICATIONS OF THE R-MRC-WPT SYSTEM

Parameters	Values	Parameters	Values
Coil structure	Spiral	DIS	0–2 m
Wire material	Copper	MIS	0–0.6 m
R_S , R_L	50 Ω	DL_1 = $2r_{\_1}$	54 cm
Coil turns (*N*coil)	5	DL_2 = $2r_{\_2}$	48 cm
Dcoil = $2R_{\text{outer}}$	60 cm	DL_3 = $2r_{\_3}$	44 cm
Pitch	1.5 cm	DL_4 = $2r_{\_4}$	38 cm
*r*coil	1.3 mm	DL_5 = $2r_{\_5}$	30 cm
*r*loop	1.3 mm	DL_6 = $2r_{\_6}$	26 cm
R_{outer}	30 cm	R_{inner}	24 cm
dlc	5 cm	-	-

$$k_{lc\_i} = \frac{\sum_{b=1}^{b=n_2} \left[\frac{\mu_0 \pi r_i^2 r_b^2}{2(r_i^2 + r_b^2 + d_{lc}^2)^{3/2}} \left(1 + \frac{15}{32}\gamma_b^2 + \frac{315}{1024}\gamma_b^4 \right) \right]}{\sqrt{\left\{ \mu_0 \mu_r r_i \left[In\left(\frac{16 r_i}{d} \right) - 2 \right] \right\} \left\{ \sum_{b=1}^{n_2} \mu_0 \mu_r r_b \left[In\left(\frac{16 r_b}{d} \right) - 2 \right] + 2 \sum_{a=1}^{n_2-1} \sum_{b=a+1}^{n_2} \left[\frac{\mu_0 \pi r_a^2 r_b^2}{2(r_a^2 + r_b^2)^{3/2}} \left(1 + \frac{15}{32}\gamma_{ab}^2 + \frac{315}{1024}\gamma_{ab}^4 \right) \right] \right\}}}. \tag{18}$$

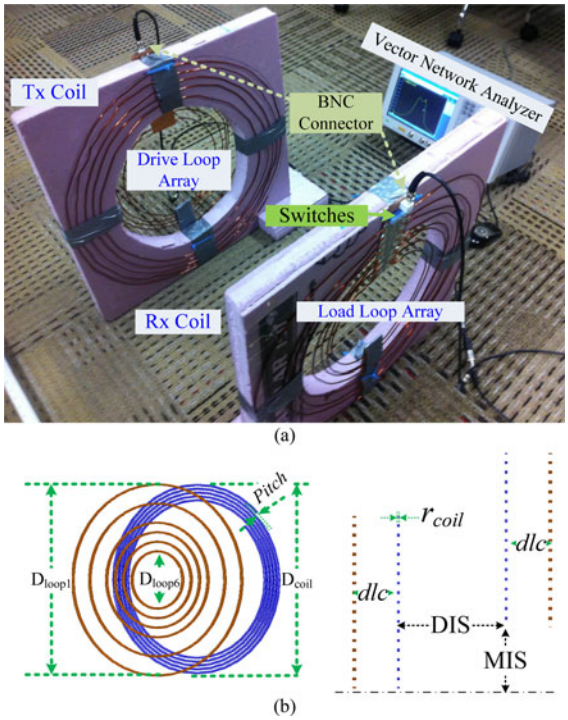

Fig. 4. (a) Proof-of-concept prototype of the R-MRC-WPT system and (b) parameter specifications.

proportional to r_i when $0 < r_i \leq 27$ cm. When 27 cm $< r_i \leq$ 30 cm, k_{lc_i} drops slightly. It should be noted that 27 cm is equal to $(R_{\text{outer}} + R_{\text{inner}})/2$, where R_{outer} is the outer radius of the spiral coil and R_{inner} is the inner radius of the spiral coil. Therefore, the maximum theoretical radius of the drive/load loop which guarantees that k_{lc_i} is directly proportional to r_i is $r_{\max} = (R_{\text{outer}} + R_{\text{inner}})/2$. This leads to the conclusion that k_{lc_i} is directly proportional to r_i when $0 < r_i \leq r_{\max}$.

In addition to the results obtained from the analytical model, k_{lc_i} as a function of r_i is also measured from the experimental prototype by using the inductance aiding method as given by (19) and the k-compensation method as given by (20) [11]. The mathematical proofs for (19) and (20) are shown in Appendix II and III, respectively. All of the inductance values in (19) are measured using the impedance analysis function of the vector network analyzer (VNA E5061B). When (20) is utilized, an SMA 100-A signal generator is used to inject a sinusoidal voltage wave into the coil, a Tektronix P5205 differential probe is used to measure the open-circuit voltage across the loop array, and a Tektronix TCP A300 current probe is used to measure currents. It can be observed that the experimental measurements shown in Fig. 3 agree with the results obtained from the analytical model

$$k_{lc\_i} = \frac{L_{\text{aid}\_i} - (L_{\text{coil}} + L_{\text{loop}\_i})}{2\sqrt{L_{\text{coil}} L_{\text{loop}\_i}}} \tag{19}$$

$$k_{lc\_i} = \sqrt{\frac{V_{2oc} \times I_{2sc}}{V_{1oc} \times I_{1sc}}}\Bigg|_i . \tag{20}$$

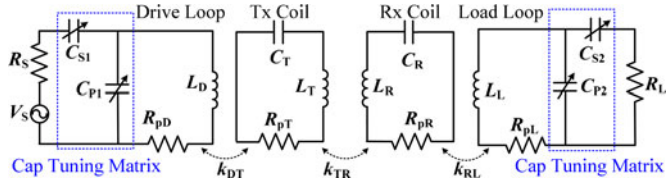

Fig. 5. Circuit diagram of the four-coil MRC-WPT system using capacitor tuning (cap-tuning system).

Next, the relationship between k_{lc_i} and transmission efficiency (η_i) is discussed. η_i is derived as in (12-2). In order to clearly observe the relationship between k_{lc_i} and η_i, (12-2) is rewritten as (12-3), which shows that η_i is directly proportional to k_{lc_i}. Due to the fact that k_{lc_i} is directly proportional to r_i when $0 < r_i \leq r_{\max}$, r_i is directly proportional to η_i.

In order to understand the relationship between k_{lc_i} and DIS_*i*, it is important to recall the definition of the critical coupling factor k_{c_i} given in Section II-B of this section (k_{c_i} is the smallest Tx to Rx coil coupling factor (k_{TR}) within which the system is able to maintain nearly constant η_i when configuration-*i* is selected). Since k_{TR} is inversely proportional to DIS^3 [12], [13], a smaller k_{c_i} is desired in order to achieve a longer DIS_*i*. It can be observed from (11) that k_{lc_i} is directly proportional to k_{c_i}, and therefore, a smaller k_{lc_i} results in a longer DIS_*i*. Due to the fact that both k_{lc_i} and L_{loop_i} are directly proportional to r_i, a smaller r_i results in a longer transmission distance DIS_*i*.

It can be concluded from the analytical model analysis that r_i is directly proportional to η_i but inversely proportional to DIS_*i*. Therefore, by switching between different configurations, i.e., different sizes of drive/load loops, higher transmission efficiency can be achieved for different ranges of distances.

III. Proof-of-Concept Experimental Prototype Results

A. System Descriptions

A proof–of-concept experimental prototype [see Fig. 4(a)] is developed to study and validate the presented method of the R-MRC-WPT system and to obtain preliminary experimental results. The prototype parameter specifications are shown in Fig. 4(b) and Table II. There are six drive loops in the drive loop array and six corresponding load loops in the load loop array. Each drive loop and its corresponding load loop are equal in size and similar in design (symmetrical system). The drive loop array and the load loop array are connected to two separate switch arrays which are able to turn ON one drive loop and a corresponding load loop at the same time. BNC connectors provide interfaces to the external circuits. A vector network analyzer (VNA E5061B) is used for measuring the transmission efficiencies of the R-MRC-WPT system under various distances and misalignment conditions. Configuration-*i* is abbreviated as Config-*i* in the rest of this paper, where $i = 1, 2, \ldots, 6$.

In the next two sections, the R-MRC-WPT system performance is evaluated by obtaining experimental measurements and is compared to a C-MRC-WPT system [where there exists only DL_2 and LL_2 in the system of Fig. 1(a)] and another

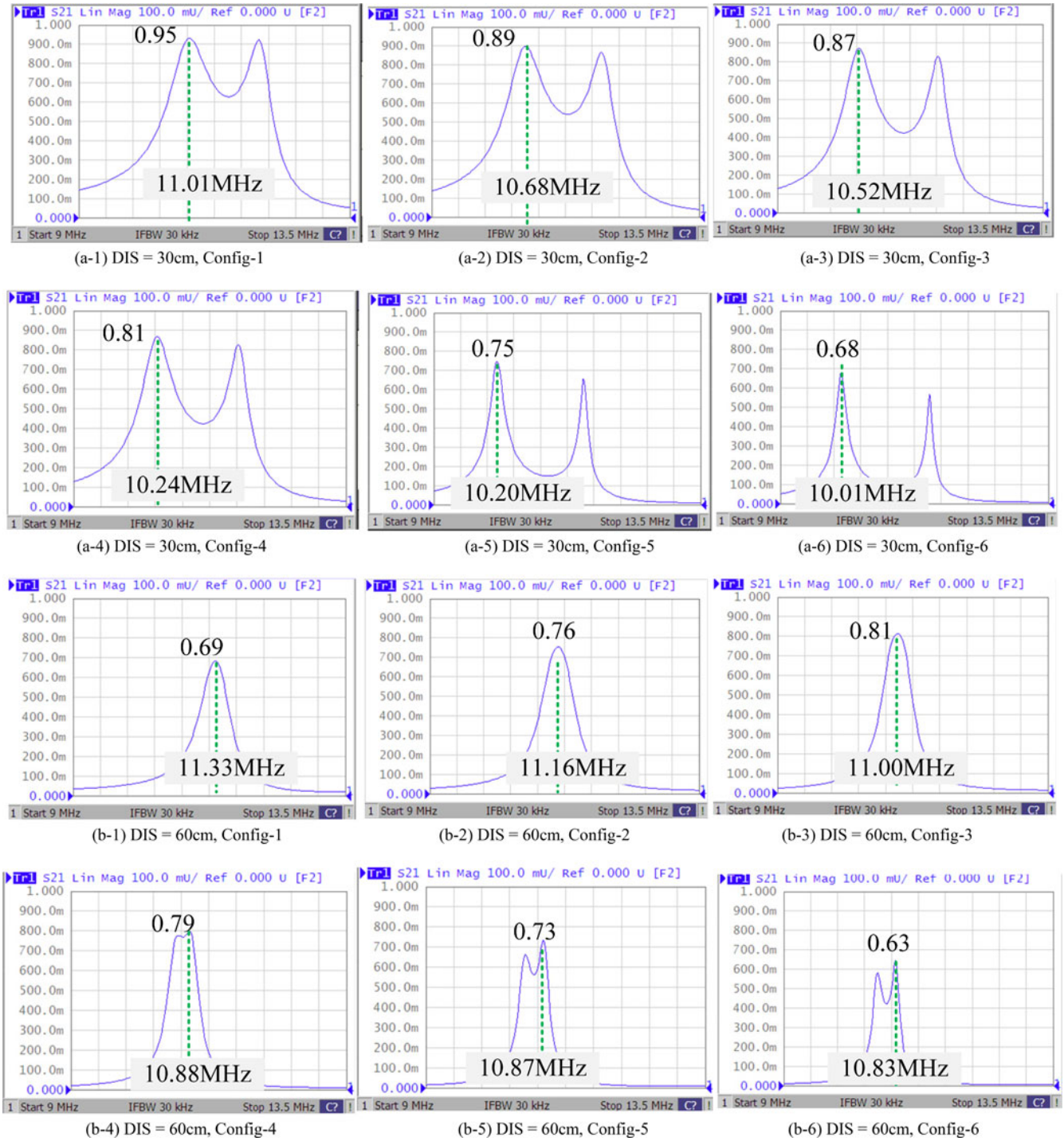

Fig. 6. $|S_{21}|$ as a function of frequency at (a) DIS = 30 cm and (b) DIS = 60 cm.

system using the capacitor tuning matrix (where there exists only DL_2 and LL_2 as well), which is abbreviated as cap-tuning system (see Fig. 5) in the rest of this paper.

B. DIS Variation

In this section, the presented experimental measurements and comparisons are for when MIS = 0 and DIS is changing from 0 to 2 m with 10-cm steps. Transmission efficiencies of the R-MRC-WPT system when selecting different configurations (from config-1 to config-6) are calculated based on (8) from measured data using VNA. Fig. 6 shows selected measurement results when DIS = 30 cm [see Fig. 6(a)] and DIS = 60 cm [see Fig. 6(b)]. It can be observed that when DIS = 30 cm, frequency splitting exists in all six configurations. The peak value of $|S_{21}|$

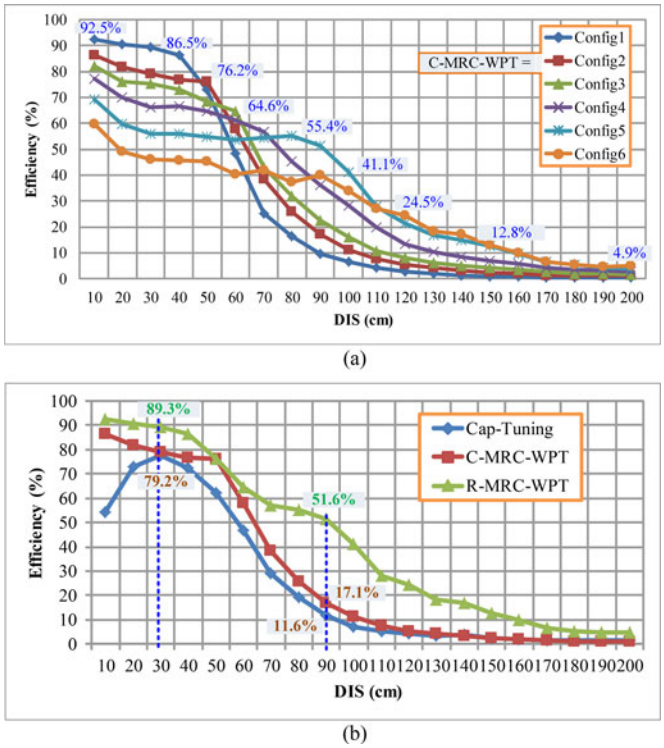

Fig. 7. Transmission efficiency as a function of DIS when Tx and Rx are perfectly aligned. (a) Transmission efficiency under different configurations and (b) transmission efficiency curves for the C-MRC-WPT, R-MRC-WPT, and cap-tuning systems.

decreases gradually from 0.95 to 0.68 as the configuration is changed from config-1 to config-6. Therefore, config-1 has the highest efficiency at DIS = 30 cm compared to the other configurations. When DIS = 60 cm, there is no frequency splitting in config-1, config-2, and config-3, while there exists frequency splitting in the rest of the configurations. The value of $|S_{21}|$ first increases and then decrease when switching from config-1 to config-6. The highest efficiency for DIS = 60 cm is obtained when using config-3.

Transmission efficiency as a function of the DIS is plotted in Fig. 7. It can be observed from Fig. 7(a) that config-1 yields the highest efficiency (∼90%) for the short distance range of 0–50 cm. Config-2 yields the highest efficiency (∼75%) for the range of 50–55 cm. Config-3 yields the highest efficiency (∼65%) for the range of 55–65 cm. Config-4 yields the highest efficiency (∼60%) for the range of 65–70 cm. Config-5 yields the highest efficiency for the range of 70–110 cm. From 70 to 90 cm, an efficiency value of ∼55% is maintained since config-5 is still in the overcoupled region for this distance range. From 90 to 110 cm, efficiency drops from ∼55% to ∼28% because the system lies in the undercoupled region for this distance range. Config-6 yields the highest efficiency for a relatively long distance range of 110–200 cm and efficiency drops from ∼28% at 110 cm to ∼4.9% at 200 cm. It can be observed that each configuration has highest transmission efficiency for a given distance range and therefore by switching between the different configurations transmission distance can be extended with higher efficiency.

In the R-MRC-WPT system, maximum achievable efficiency at different DIS values can adaptively be tracked while reconfiguring the system such that transmission efficiencies within all DIS ranges are improved. The efficiency curve obtained from the R-MRC-WPT system is compared to the efficiency curves obtained from the C-MRC-WPT system and the Cap-tuning system as shown in Fig. 7(b). It can be observed that the transmission efficiency of the R-MRC-WPT system is the highest at every point and the transmission efficiency of the cap-tuning system is the lowest at every point when DIS ranges from 0 to 2 m. When compared to the C-MRC-WPT system at DIS = 30 cm, the R-MRC-WPT system improves the efficiency by 10.1%. At DIS = 90 cm, efficiency is improved by 34.5%. If one of the system configurations, for example, config-5, is removed from the R-MRC-WPT system, system efficiency in the range of 70 cm < DIS < 90 cm would drop from ∼55% to ∼40%. In other words, the larger the number of configurations used, the higher the transmission efficiency improvement can be obtained for the DIS ranges.

C. R-MRC-WPT System With Lateral Misalignment

In this section, the presented experimental measurements and comparisons are for the R-MRC-WPT system when varying MIS values from 0 to 60 cm with 10-cm steps at fixed DIS of 40 and 50 cm. The transmission efficiency experimental measurement results as a function of the MIS when DIS = 40 cm are plotted in Fig. 8(a). It can be observed that config-1 yields the highest efficiency for the MIS range of 0–30 cm. From 0 to 20 cm, an efficiency value of ∼80% is maintained since config-1 operates in the overcoupled region for this MIS range. When Rx position changes from MIS = 20 cm to MIS = 30 cm while using config-1, efficiency drops from 80% to 60%. This indicates that the operation of config-1 moved to the undercoupled region when MIS > 20 cm. The results obtained as shown in Fig. 8(a) show that config-2 does not yield to a highest efficiency for any MIS range. Config-3 yields the highest efficiency for the MIS range of 30–38 cm. Config-4 yields the highest efficiency for the range of 38–50 cm. Config-5 yields the highest efficiency for the range of 50–60 cm. As it is the case for config-2, config-6 does not yield to a highest efficiency for any MIS range. Each of the other four configurations (config-1, config-3, config-4, and config-5) provides highest transmission efficiency for a given range of MIS.

The resulted transmission efficiency curve of the R-MRC-WPT system is shown in Fig. 8(b), and is compared to the efficiency curves of the C-MRC-WPT and the cap-tuning systems. It can be observed that transmission efficiency of the R-MRC-WPT system is the highest and transmission efficiency of the cap-tuning system is the lowest. When compared to the C-MRC-WPT system at MIS = 20 cm, the R-MRC-WPT system improves the transmission efficiency by 8.8%. At MIS = 40 cm, transmission efficiency is improved by 9.8%.

Experimental measurements and analysis are also performed for the case when varying MIS while fixing DIS at 50 cm. The transmission efficiency as a function of the MIS is plotted in Fig. 9(a). It can be observed that config-1 does not yield

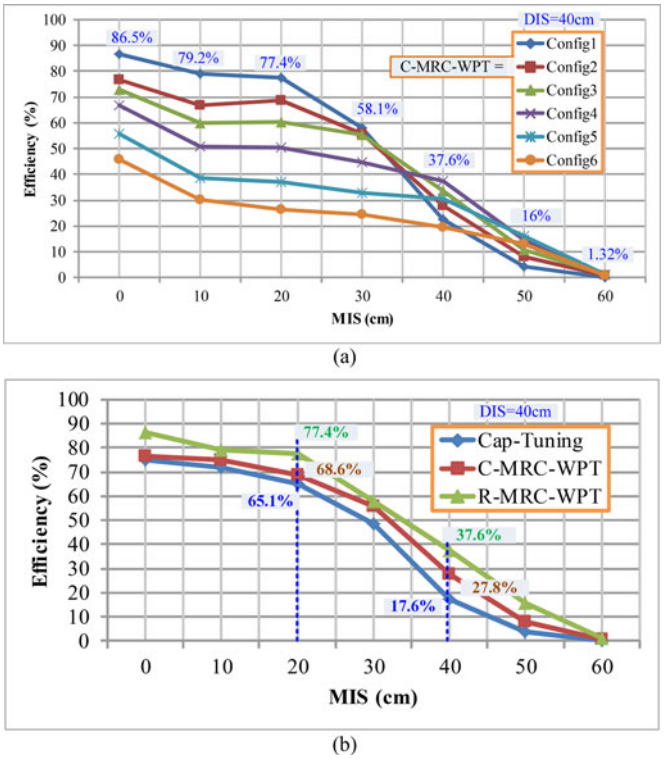

Fig. 8. Transmission efficiency as a function of lateral misalignment (MIS) when DIS = 40 cm. (a) Transmission efficiency under different configurations and (b) transmission efficiency curves for the C-MRC-WPT, R-MRC-WPT, and cap-tuning systems.

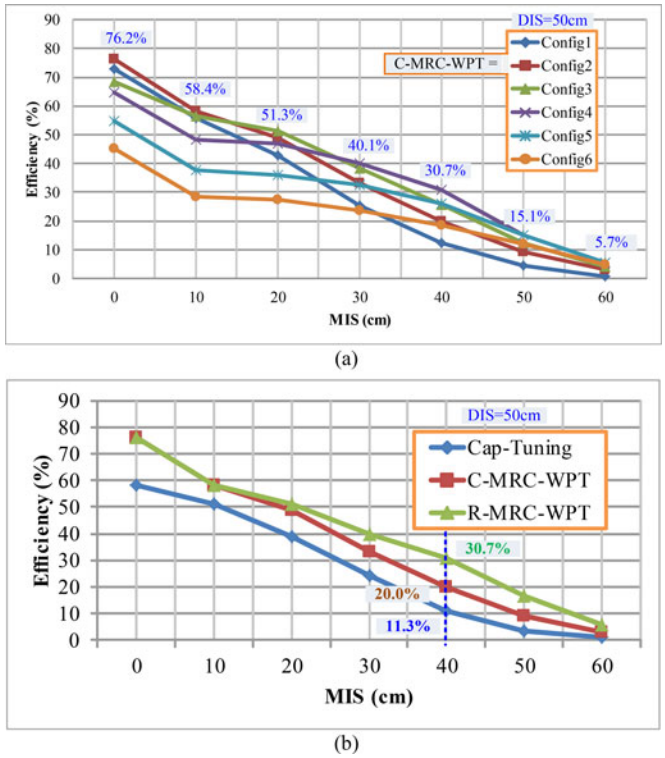

Fig. 9. Transmission efficiency as a function of lateral misalignment (MIS) when DIS = 50 cm. (a) Transmission efficiency under different configurations and (b) transmission efficiency curves for the C-MRC-WPT, R-MRC-WPT, and Cap-tuning systems.

highest efficiency for any MIS range. This is because when DIS = 50 cm and MIS = 0, config-1 already operates in the undercoupled region and its transmission efficiency drops down rapidly when DIS and/or MIS further increases. Config-2 yields the highest efficiency for the MIS range of 0–15 cm. Config-3 yields the highest efficiency of ∼50% for the MIS range of 15–25 cm. Config-4 yields the highest efficiency for the MIS range of 30–50 cm. Config-5 yields the highest efficiency for the range of 50–60 cm. As it is the case for config-1, config-6 does not yield the highest efficiency for any MIS range. It can be observed that each of the other four configurations (config-2, config-3, config-4, and config-5) can improve the transmission efficiency for a given range of MIS.

The resulting transmission efficiency curve of the R-MRC-WPT system is compared to the efficiency curves of the C-MRC-WPT and the cap-tuning systems in Fig. 9(b). It can be observed that transmission efficiency of the R-MRC-WPT system is the highest and transmission efficiency of the cap-tuning system is the lowest. When compared with C-MRC-WPT system at MIS = 40 cm, the R-MRC-WPT system improves the transmission efficiency by 10.7%. Similar to the case when DIS is varied, the larger the number of configurations is, the higher the transmission efficiency improvement can be obtained for the MIS ranges.

From efficiency comparisons previously mentioned, it can be concluded that the cap-tuning system can approach the maximum possible efficiency only at a given DIS or MIS value for the fixed design structure, while switching between different loops reconfigures the system such that it switches between different designs or operating/efficiency curves that are more optimized for different conditions with higher efficiency values.

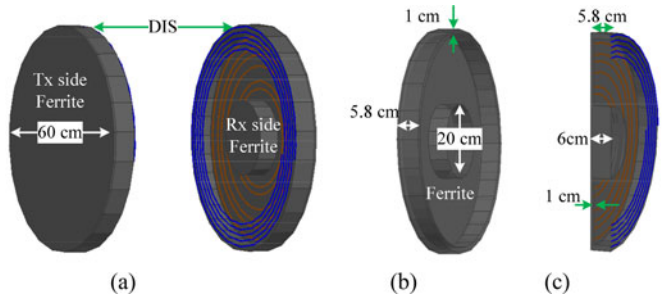

Fig. 10. (a) Three-dimensional model of the R-MRC-WPT system with ferrite structure on Tx side and Rx side, (b) three-dimensional view of ferrite structure, and (c) cross-sectional view of the Tx side structure.

IV. Additional Comments

A. *Use of Ferrite With the R-MRC-WPT System*

This section presents preliminary investigation on the use of the ferrite material in the R-MRC-WPT system by using the ANSYS HFSS 3-D physical model simulations. Fig. 10 shows the 3-D model of the R-MRC-WPT system with ferrite structure used for both the Tx side and the Rx side. The properties of the

TABLE III
PROPERTIES OF THE FERRITE MATERIAL USED IN THE R-MRC-WPT SYSTEM

Property	Value
Material Type	4F1 [37]
Saturation Flux density	0.32T
Resistivity	$\sim 10^5\ \Omega\cdot$m
Magnetic Loss Tangent	0.00035
Relative Permeability	300
Relative Permittivity	15
Mass Density	4600 kg/m^3

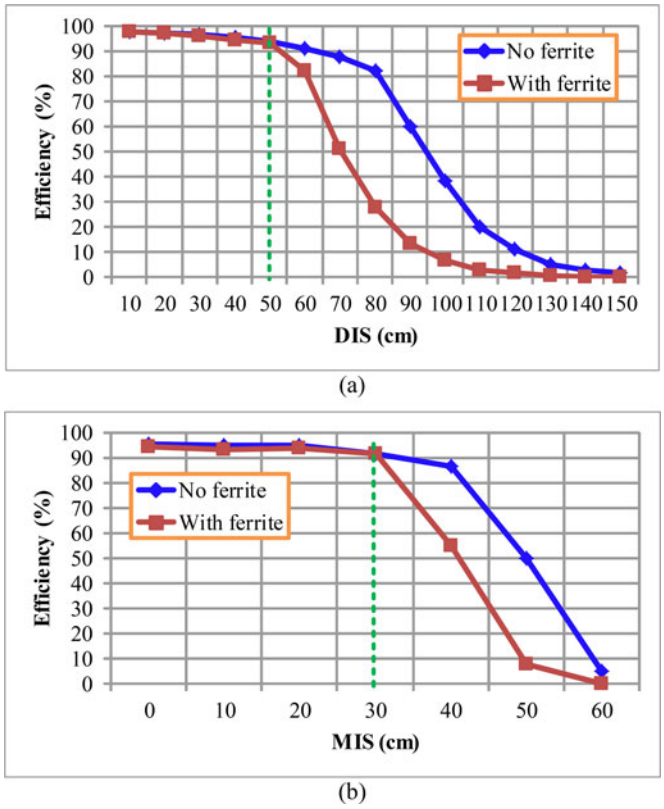

Fig. 11. Comparison between transmission efficiency values for the R-MRC-WPT system with and without ferrite structure for (a) different DIS and (b) different MIS (with DIS = 40 cm) conditions.

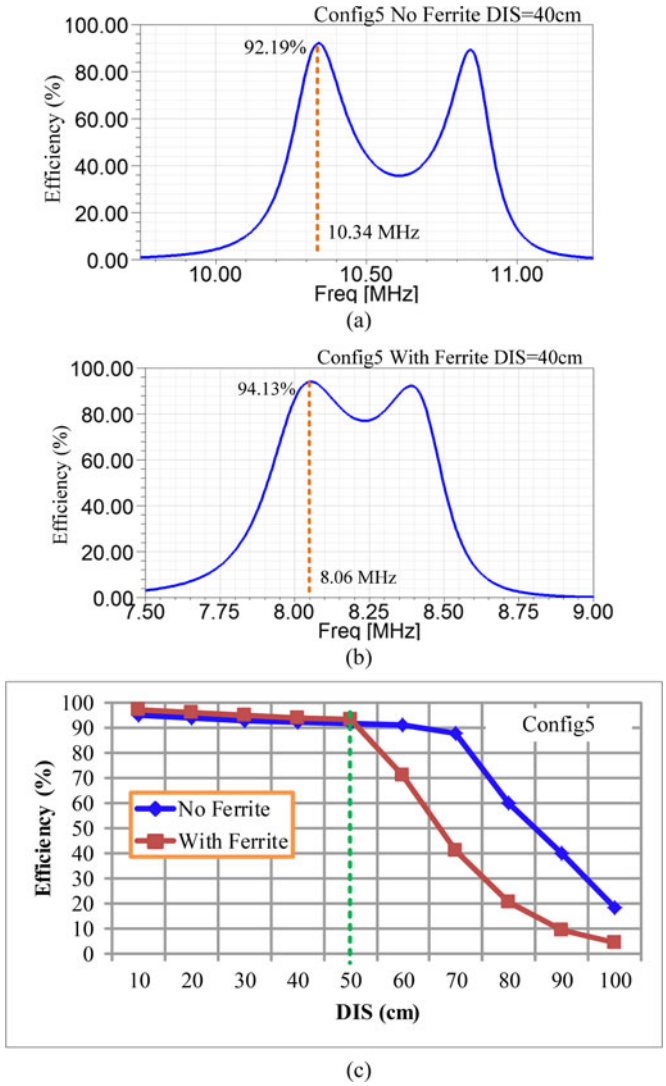

Fig. 12. Comparison between transmission efficiency values for the Config-5 (a) without ferrite structure at DIS = 40 cm, (b) with ferrite structure when DIS = 40 cm, and (c) under different DIS conditions.

ferrite material used in the simulation are shown in Table III. Results for transmission efficiency values for the R-MRC-WPT system with and without ferrite material for different DIS and MIS (while DIS = 40 cm) conditions are shown in Fig. 11 for comparison. It can be observed that the R-MRC-WPT system with and without ferrite has almost the same transmission efficiency for small DIS values ($\leq$50 cm) and for small MIS values ($\leq$30 cm). When DIS and MIS increase, the R-MRC-WPT system without ferrite has larger transmission efficiency.

However, the results in Fig. 11 do not mean that the ferrite has no effect on the four-coil MRC-WPT system. For example, in Fig. 12(a) and (b), the operation frequency of Config-5 without ferrite (10.34 MHz) is $\sim$2.5 MHz higher than that with ferrite (8.06 MHz). This is because ferrite has much higher relative permeability ($\sim$300 in this design) than air ($\sim$1), and therefore, effective inductance/mutual inductance values of the coils increase and self-resonance frequency of Tx/Rx coil decreases according to (2). Transmission efficiencies with and without ferrite for Config-5 under various DIS conditions are compared in Fig. 12(c), which shows that the transmission efficiency with ferrite is slightly higher than that without ferrite at close distance (DIS $\leq$ 50 cm). When DIS increases, efficiency of Config-5 without ferrite is higher than that with ferrite. Therefore, it is possible to increase the transmission efficiency of the four-coil MRC-WPT system at shorter distances by adding ferrite structure while decreasing transmission efficiency at longer distances.

The use of ferrite structure might achieve larger transmission efficiency improvement at shorter distances for a two-coil system [7]–[14]. However, in the R-MRC-WPT system, the transmission efficiency has already been improved as a result of reconfiguring the system such that only a smaller improvement can be achieved at shorter distances when using the ferrite structure.

B. Use of Litz Wire With the R-MRC-WPT System

The litz wire is designed to reduce the skin effect and proximity effect losses in conductors used at high frequencies. Commercially available litz wires can operate with frequencies up to 2.8 MHz [38]. Even though 2.8 MHz is lower than the operation frequency of the R-MRC-WPT system presented in this paper (which is higher than 10 MHz), higher transmission efficiency might be obtained by using the litz wire. This topic is a candidate for future investigation.

V. Conclusion

The paper presented a method for the R-MRC-WPT system that adapts the reconfiguration of the four-coil WPT system in order to improve transmission efficiency under various transmission distances and misalignment conditions. The reconfigurability of the system is realized by adaptively switching between different sizes of drive loops and load loops, which does not result in the disadvantages that exist in the mechanical tuning method such as volume increase and requirement of mechanical movements. Theoretical basis for the presented method are devised from a circuit model and an analytical model and are validated by using a proof-of-concept experimental prototype results. Experimental results show that the R-MRC-WPT system has better performances than the C-MRC-WPT system and cap-tuning system in terms of transmission efficiency, transmission distance, and misalignment tolerance. Analysis also shows that when a larger number of configurations are used in the system, higher efficiency improvement can be achieved under various DIS and/or MIS conditions.

While this paper focuses on presenting the R-MRC-WPT system for low-power applications such as consumer electronics, the concept is candidate for higher power levels. However, there might be health and safety concerns [11] above certain power levels especially that the presented system transmits power for distances that are larger than one coil diameter. Future work includes but is not limited to developing and implementing adaptive control algorithms to automatically realize the system reconfigurability.

Appendix I

A general two-port network is shown in Fig. 13, where a_1 and a_2 are incident waves, and b_1 and b_2 are reflected waves. a_1 and b_2 are defined in (A1) and (A2), respectively [39]. In this paper, $Z_s = Z_L = Z_0 = 50\ \Omega$

$$a_1 = \frac{V_1 + I_1 Z_0}{2\sqrt{Z_0}} \tag{A1}$$

$$b_2 = \frac{V_2 - I_2 Z_0}{2\sqrt{Z_0}}. \tag{A2}$$

From the definition of S_{21}, the following can be obtained:

$$S_{21} = \left.\frac{b_2}{a_1}\right|_{a_2=0} = \frac{\frac{V_2 - I_2 Z_0}{2\sqrt{Z_0}}}{\frac{V_1 + I_1 Z_0}{2\sqrt{Z_0}}} = \frac{V_2 - (-V_2)}{V_S} = \frac{2V_2}{V_S}. \tag{A3}$$

According to the maximum power transfer theorem [40], the maximum available power (P_A) at port one of the two-port network is given by

$$P_A = \left(\frac{1}{2}V_S\right)^2 / Z_0. \tag{A4}$$

Therefore, the transmission efficiency of the two-port network is

$$\eta = \frac{P_L}{P_A} = \frac{V_2^2/Z_L}{\left(\frac{1}{2}V_S\right)^2/Z_0} = 4\frac{V_2^2}{V_S^2} = S_{21}^2. \tag{A5}$$

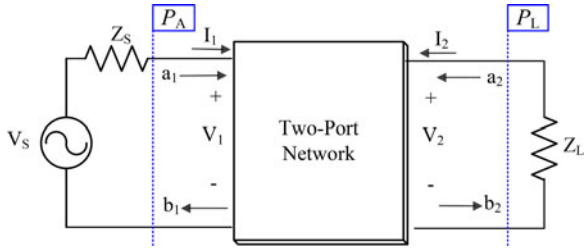

Fig. 13. General two-port network.

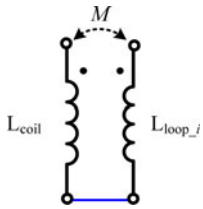

Fig. 14. Equivalent circuit model of directly coupled inductors that are connected in series.

Appendix II

When L_{coil} and $L_{\text{loop\_}i}$ are connected in series and are directly coupled as shown in Fig. 14, the equivalent inductance L_{aid_i} is given by (A6) [40]

$$L_{\text{aid\_}i} = L_{\text{coil}} + L_{\text{loop\_}i} + 2M. \tag{A6}$$

Therefore, the mutual inductance between L_{coil} and $L_{\text{loop\_}i}$ is given by

$$M = \frac{L_{aid\_i} - (L_{\text{coil}} + L_{\text{loop\_}i})}{2}. \tag{A7}$$

Based on (1) and (A7), k_{lc_i} can be calculated as

$$k_{lc\_i} = \frac{M_{lc}}{\sqrt{L_{\text{coil}} L_{\text{loop\_}i}}} = \frac{L_{\text{aid\_}i} - (L_{\text{coil}} + L_{\text{loop\_}i})}{2\sqrt{L_{\text{coil}} L_{\text{loop\_}i}}}. \tag{A8}$$

Appendix III

From Fig. 15, (A9) can be derived using circuit analysis [40]

$$\begin{cases} v_1(t) = L_{\text{coil}}\frac{di_1}{dt} - M\frac{di_2}{dt} \\ v_2(t) = -M\frac{di_1}{dt} + L_{\text{loop\_}i}\frac{di_2}{dt} \end{cases}. \tag{A9}$$

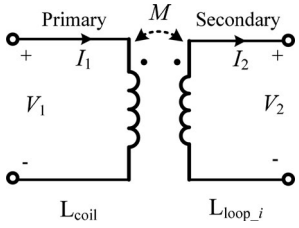

Fig. 15. Equivalent circuit model of a coupled inductor.

When the secondary side is an open circuit, $I_2 = 0$ and (A9) can be rewritten as

$$\begin{cases} v_{1oc}(t) = L_{\text{coil}} \frac{di_{1oc}}{dt} \\ v_{2oc}(t) = -M \frac{di_{1oc}}{dt} \end{cases}. \tag{A10}$$

When the secondary side is shorted (short circuit), $V_2 = 0$. Therefore,

$$L_{\text{loop\_}i} \times I_{2sc} = M \times I_{1sc}. \tag{A11}$$

From (A10) and (A11), the following can be obtained:

$$\begin{cases} \left| \frac{V_{2oc}}{V_{1oc}} \right| = \frac{M}{L_{\text{coil}}} \\ \left| \frac{I_{2sc}}{I_{1sc}} \right| = \frac{M}{L_{\text{loop\_}i}} \end{cases}. \tag{A12}$$

Thus, using (1) and (A12)

$$k_{lc\_i} = \frac{M_{lc}}{\sqrt{L_{\text{coil}} L_{\text{loop\_}i}}} = \sqrt{\frac{V_{2oc} \times I_{2sc}}{V_{1oc} \times I_{1sc}}}\Bigg|_i. \tag{A13}$$

REFERENCES

[1] J. Kim, H. Son, D. Kim, and Y. Park, "Optimal design of a wireless power transfer system with multiple self-resonators for an LED TV," *IEEE Trans. Consum. Electron.*, vol. 58, no. 3, pp. 775–780, Aug. 2012.

[2] R. Wu, W. Li, H. Luo, J. K. O. Sin, and C. C. Yue, "Design and characterization of wireless power links for brain-machine interface applications," *IEEE Trans. Power Electron.*, vol. 29, no. 10, pp. 5462–5471, Oct. 2014.

[3] W. Chwei-Sen, O. H. Stielau, and G. A. Covic, "Design considerations for a contactless electric vehicle battery charger," *IEEE Trans. Ind. Electron.*, vol. 52, no. 5, pp. 1308–1314, Oct. 2005.

[4] G. A. Landis, "Reevaluating satellite solar power systems for earth," in *Proc. IEEE 4th World Conf. Photovoltaic Energy Convers.*, May 7–12, 2006, pp. 1939–1942.

[5] A. Sahai and D. Graham, "Optical wireless power transmission at long wavelengths," in *Proc. Int. Conf. Space Opt. Syst. Appl.*, May 11–13, 2011, pp. 164–170.

[6] N. Tesla, "System of transmission of electrical energy," U.S. Patent 645 576, Mar. 20, 1900.

[7] U. K. Madawala and D. J. Thrimawithana, "A bidirectional inductive power interface for electric vehicles in V2G systems," *IEEE Trans. Ind. Electron.*, vol. 58, no. 10, pp. 4789–4796, Oct. 2011.

[8] M. G. Eagen, D. L. O'Sullivan, J. G. Hayes, M. J. Willers, and C. P. Henze, "Power factor corrected single stage inductive charger for electric vehicle batteries," *IEEE Trans. Ind. Electron.*, vol. 54, no. 2, pp. 1217–1226, Apr. 2007.

[9] G. A. Covic, J. T. Boys, M. L. G. Kissin, and H. G. Lu, "A three-phase inductive power transfer system for roadway-powered vehicles," *IEEE Trans. Ind. Electron.*, vol. 54, no. 6, pp. 3370–3378, Dec. 2007.

[10] M. Budhia, G. A. Covic, and J. T. Boys, "Design and optimization of circular magnetic structures for lumped inductive power transfer systems," *IEEE Trans. Power Electron.*, vol. 26, no. 11, pp. 3096–3108, Nov. 2011.

[11] O. C. Onar, J. M. Miller, S. L. Campbell, C. Coomer, C. P. White, and L. E. Seiber, "Oak ridge national laboratory wireless power transfer development for sustainable campus initiative," in *Proc. IEEE Transp. Electrification Conf. Expo.*, Jun. 2013, pp. 1–8.

[12] J. M. Miller, O. C. Onar, and M. Chinthavali, "Primary-side power flow control of wireless power transfer for electric vehicle charging," *IEEE J. Emerg. Sel. Topics Power Electron.*, vol. 3, no. 1, pp. 147–162, Mar. 2015.

[13] S. Y. Choi, J. Huh, W. Y. Lee, and C. T. Rim, "Asymmetric coil sets for wireless stationary EV chargers with large lateral tolerance by dominant field analysis," *IEEE Trans. Power Electron.*, vol. 29, no. 12, pp. 6406–6420, Dec. 2014.

[14] J. Lee and B. Han, "A bidirectional wireless power transfer EV charger using self-resonant PWM," *IEEE Trans. Power Electron.*, vol. 30, no. 4, pp. 1784–1787, Apr. 2015.

[15] S. Hui, W. Zhong, and C. Lee, "A critical review of recent progress in mid-range wireless power transfer," *IEEE Trans. Power Electron.*, vol. 29, no. 9, pp. 4500–4511, Sep. 2014.

[16] A. Kurs, A. Karalis, R. Moffatt, J. D. Joannopoulos, P. Fisher, and M. Soljačíc, "Wireless power transfer via strongly coupled magnetic resonances," *Science*, vol. 317, no. 5834, pp. 83–86, Jul. 2007.

[17] A. P. Sample, D. A. Meyer, and J. R. Smith, "Analysis, experimental results, and range adaptation of magnetically coupled resonators for wireless power transfer," *IEEE Trans. Ind. Electron.*, vol. 58, no. 2, pp. 544–554, Feb. 2011.

[18] Z. Dang and J. A. Abu Qahouq, "Modeling and investigation of magnetic resonance coupled wireless power transfer system with lateral misalignment," in *Proc. IEEE Appl. Power Electron. Conf.*, Mar. 2014, pp. 1317–1322.

[19] Z. Dang and J. A. Abu Qahouq, "Modelling and simulation of magnetic resonance coupled wireless power transfer systems," *Int. Rev. Model. Simul.*, vol. 6, no. 5, pp. 1607–1617, Oct. 2013.

[20] Z. Dang and J. A. Abu Qahouq, "Range and misalignment tolerance comparisons between two-coil and four-coil wireless power transfer systems," in *Proc. IEEE Appl. Power Electron. Conf.*, Mar. 2015, pp. 1234–1240.

[21] Z. Dang and J. A. Abu Qahouq, "Elimination method for the transmission efficiency valley of death in laterally misaligned wireless power transfer systems," in *Proc. IEEE Appl. Power Electron. Conf.*, Mar. 2015, pp. 1644–1649.

[22] Y. Zhang, Z. Zhao, and K. Chen, "Frequency decrease analysis of resonant wireless power transfer," *IEEE Trans. Power Electron.*, vol. 29, no. 3, pp. 1058–1063, Mar. 2014.

[23] Y. Lim, H. Tang, S. Lim, and J. Park, "An adaptive impedance-matching network based on a novel capacitor matrix for wireless power transfer," *IEEE Trans. Power Electron.*, vol. 29, no. 8, pp. 4403–4413, Aug. 2014.

[24] W. M. Ng, C. Zhang, D. Lin, and S. Y. R. Hui, "Two- and three-dimensional omnidirectional wireless power transfer," *IEEE Trans. Power Electron.*, vol. 29, no. 9, pp. 4475–4478, Sep. 2014.

[25] J. Yin, D. Lin, C. Lee, and S. Y. R. Hui, "A systematic approach for load monitoring and power control in wireless power transfer systems without any direct output measurement," *IEEE Trans. Power Electron.*, vol. 30, no. 3, pp. 1657–1667, Mar. 2015.

[26] W. Zhong, C. Zhang, X. Liu, and S. Y. R. Hui, "A methodology for making a three-coil wireless power transfer system more energy efficient than a two-coil counterpart for extended transfer distance," *IEEE Trans. Power Electron.*, vol. 30, no. 2, pp. 933–942, Feb. 2015.

[27] B. L. Cannon, J. F. Hoburg, D. D. Stancil, and S. C. Goldstein, "Magnetic resonant coupling as a potential means for wireless power transfer to multiple small receivers," *IEEE Trans. Power Electron.*, vol. 24, no. 7, pp. 1819–1825, Jul. 2009.

[28] H. Li, J. Li, K. Wang, W. Chen, and X. Yang, "A maximum efficiency point tracking control scheme for wireless power transfer systems using magnetic resonant coupling," *IEEE Trans. Power Electron.*, vol. 30, no. 7, pp. 3998–4008, Aug. 2014.

[29] C. Zhang, W. Zhong, X. Liu, and S. Y. R. Hui, "A fast method for generating time-varying magnetic field patterns of mid-range wireless power transfer systems," *IEEE Trans. Power Electron.*, vol. 30, no. 3, pp. 1513–1520, Mar. 2015.

[30] S. Aldhaher, P. C.-K. Luk, and J. F. Whidborne, "Electronic tuning of misaligned coils in wireless power transfer systems," *IEEE Trans. Power Electron.*, vol. 29, no. 11, pp. 5975–5982, Nov. 2014.

[31] L. H. Chen, S. Liu, Y. C. Zhou, and T. J. Cui, "An optimizable circuit structure for high-efficiency wireless power transfer," *IEEE Trans. Ind. Electron.*, vol. 60, no. 1, pp. 339–349, Jan. 2013.

[32] M. Kiani and M. Ghovanloo, "The circuit theory behind coupled-mode magnetic resonance-based wireless power transmission," *IEEE Trans. Circuit Syst. I: Reg. Papers*, vol. 59, no. 9, pp. 2065–2074, Sep. 2012.
[33] T. P. Duong and J. W. Lee, "Experimental results of high-efficiency resonant coupling wireless power transfer using a variable coupling method," *IEEE Microw. Wireless Compon. Lett.*, vol. 21, no. 8, pp. 442–444, Aug. 2011.
[34] Y. Zhang and Z. Zhao, "Frequency-splitting analysis of four-coil resonant wireless power transfer," *IEEE. Trans. Ind. Appl.*, vol. 50, no. 4, pp. 2436–2445, Jul. 2014.
[35] F. W. Grover, *Inductance Calculations: Working Formulas and Tables*, New York, NY, USA: Dover, 1946, p. 134.
[36] S. Raju, R. Wu, M. Chan, and C. Yue, "Modeling of mutual coupling between planar inductors in wireless power applications," *IEEE Trans. Power Electron.*, vol. 29, no. 1, pp. 481–490, Jan. 2014.
[37] Ferroxcube. (2013, Jul.). Soft Ferrite and Accessories Data Handbook. [Online]. Available: http://www.ferroxcube.com/FerroxcubeCorporateReception/datasheet/FXC_HB2013.pdf
[38] New England Wire Technologies, (2015, Apr.). [Online]. Available: http://www.newenglandwire.com/products/litz-wire-and-formed-cables/round.aspx
[39] J. Hong and M. J. Lancaster, *Microstrip Filters for RF/Microwave Applications*, New York, NY, USA: Wiley, July 2001.
[40] J. D. Irwin and R. M. Nelms, *Basic Engineering Circuit Analysis*, 10th ed. New York, NY, USA: Wiley, Oct. 2010.

Zhigang Dang (S'14) received the B.Sc. degree in automation from Central South University, Hunan, China, in 2011, and the Master's degree from the University of Alabama, Tuscaloosa, AL, USA, in Dec. 2013, where he is currently working toward the Ph.D. degree at the Department of Electrical and Computer Engineering.

His research interests include wireless power transfer, power magnetics for switching power converters, and power management systems.

Yuan Cao (S'15) received the Bachelor's and Master's degrees in electrical engineering from Central South University, Hunan, China, in 2011 and 2014, respectively. He is currently working toward the Ph.D. degree in the Department of Electrical and Computer Engineering, University of Alabama, Tuscaloosa, AL, USA.

His research interests include wireless power transfer, battery management system, and automatic control. He is the recipient of the Graduate Council Fellowship Award at the University of Alabama in 2014.

Jaber A. Abu Qahouq (SM'07) received the B.Sc. degree (with first class Hons.) from the Princess Sumaya University for Technology/Royal Scientific Society (RSS), Amman, Jordan, in 1998, and the M.S. and Ph.D. degrees from the University of Central Florida (UCF), Orlando, FL, USA, in 2000 and 2003, respectively, all in electrical engineering and electronics.

He is currently an Associate Professor with the Department of Electrical and Computer Engineering, College of Engineering, University of Alabama, Tuscaloosa, AL, USA. Before that, he was with Intel Corporation, Hillsboro, OR, USA, UCF, and RSS. He is the author or coauthor of more than 100 refereed publications, two book chapters, and is a holder of 15 U.S. patents as of June 2014. He served as an IEEE Conference Technical Program Committee Member of the IEEE Power Electronics Specialists Conference in 2007; the IEEE International Symposium on Circuits and Systems in 2008; the IEEE International Conference on Electronics, Circuits, and Systems in 2009–2011; the IEEE Energy Conversion Congress and Exposition in 2010–2013; the IEEE Applied Power Electronics Conference and Exposition in 2013–2015; among others.

Dr. Abu Qahouq received the King of Jordan Royal Watch in 1998, the IEEE Outstanding Graduate Student Award in 2002, the Division Recognition Award from Intel Corporation in 2006, and the Institution of Engineering Technology Premium Award in 2009, among others.